Electrochimica Acta 380 (2021) 138215

Contents lists available at ScienceDirect

Electrochimica Acta

journal homepage: www.elsevier.com/locate/electacta

Trifunctional iridium-based electrocatalysts for overall water splitting and Zn-air batteries

Ning Liu[a,1], Yin Wang[b,1], Qiaoqiao Zhang[a], Jingqi Guan[a,*]

[a] Institute of Physical Chemistry, College of Chemistry, Jilin University, Changchun 130012, PR China
[b] Inner Mongolia Key Laboratory of Carbon Nanomaterials, College of Chemistry and Materials Science, Nano Innovation Institute, Inner Mongolia University for Nationalities, Tongliao 028000, China

ARTICLE INFO

Article history:
Received 13 January 2021
Revised 28 February 2021
Accepted 22 March 2021
Available online 26 March 2021

Keywords:
Carbon nanotube
Hydrogen evolution reaction
Iridium
Oxygen evolution reaction
Oxygen reduction reaction

1. Introduction

The reduction of fossil-based energy resources and ever-growing environmental pollution have stimulated the exploitation of clean and sustainable energy techniques (e.g. water electrolyzers and Zn-air batteries) [1,2]. However, sluggish kinetics of HER, OER, and ORR leads to low energy efficiency [3-5]. Although platinum-based catalysts exhibit superior HER and ORR activities, and RuO_2 and IrO_2 show high OER activity in acidic electrolytes, the infrequency and high costs of precious metals impede their commercial applications [6]. Meanwhile, single noble metal based materials fail to concurrently catalyze HER, OER, and ORR. Therefore, it is pivotal to develop high-efficiency multifunctional electrocatalysts for water electrolyzers and metal-air batteries [7,8].

To reduce the usage of precious metal-based catalysts, noble-metal-based alloys, nanoparticles, two-dimension nano materials, and composites were developed for HER, OER, or ORR [9,10]. To improve electrocatalytic OER performance of IrO_2, one of the most efficient strategies is downsizing its nanoparticles to enhance unsaturated Ir atoms on the surface, since they can easily react with water molecules to form surface hydroxy sites owing to large water binding energy [11]. In addition, more active sites and high Miller-index facets can be exposed by downsizing nanoparticles. Jaramillo et al. reported that an $IrO_x/SrIrO_3$ catalyst obtained by Sr-leaching from $SrIrO_3$ showed high OER activity in acidic media [12]. For iridium oxide, the electric conductivity depends on their chemical states. Crystalline IrO_2 particles show higher electric conductivity than amorphous hydrous iridium oxides [13]. The electric conductivity of iridium oxide can be significantly improved by supporting it onto carbonaceous materials [14]. In addition, for IrO_2, typical OER overpotential is approximately 300 mV at 10 mA cm^{-2} in acidic electrolytes [15]. To increase the electrocatalytic activity and reduce the usage of iridium, two efficient strategies (enhancing the density of active sites and intrinsic activity of Ir-based active sites) were developed. Supporting iridium oxides onto nonmetal-doped CNT (e.g. N-doped CNT) would increase the dispersion of IrO_2 to enhance the density of active sites, whereas the doped nonmetal would influence the electronic structure of IrO_2, thus improving electrocatalytic performance. However, although iridium oxide shows excellent OER activity, it is seldom investigated in HER and ORR. In this work, for the first time, we demonstrated that the iridium oxide supported on N-doped CNT exhibits superior HER activity, which can be comparable with Pt/C.

Recent research showed that M-N-C materials can efficiently catalyze ORR, especially in alkaline media [16]. The local environment of metal centers can be adjusted by the coordination of N/O/C atoms, thus influencing the catalytic activity of single-atom catalysts. However, there are seldom reports about the influence of N-doping on the catalytic behavior of IrO_2 nanoclusters and nanoparticles. A good deal of theoretical calculations and ex-

* Corresponding author.
E-mail address: guanjq@jlu.edu.cn (J. Guan).
[1] Both the authors contributed equally to this work.

https://doi.org/10.1016/j.electacta.2021.138215

periential results showed that N-doping can immensely affect the electronic cloud density of adjacent carbon atoms, thus improving ORR activity of carbon-based materials [17]. Theoretically, when the particle size of IrO_x is small enough, the interaction between iridium oxo species and N-doped carbon materials would be reinforced and the electrocatalytic performance would be enhanced [18]. In this work, we synthesized an efficient and robust trifunctional electrocatalyst by highly dispersing IrO_x onto NCNT with an Ir loading of 3 wt.%. This trifunctional electrocatalyst can be used for acidic, alkaline, and neutral overall water splitting and zinc–air batteries.

2. Experimental section

2.1. Catalyst preparation

2.1.1. Synthesis of NCNT

Multiwalled carbon nanotubes with inner diameter of 5–10 nm were refluxed in nitric acid to remove residual oxides during the synthetic procedure. After filtering, washing, and drying, the black solid was then annealed in ammonia at 750°C for 6 h to obtain N-doped CNT (NCNT). The surface nitrogen content is ca. 0.5%.

2.1.2. Synthesis of IrO_x/NCNT

$IrCl_3$ and NCNT were dispersed in water. After evaporating and drying, the mixture was reduced in 5% H_2 at 200°C for 1 h, which was tenderly oxidized in air at room temperature for 24 h to obtain IrO_x/NCNT. The content of iridium was measured to be 0.95 wt%, 1.91 wt%, 2.82 wt%, 3.65 wt%, and 4.58 wt% for 1%IrO_x/NCNT, 2%IrO_x/NCNT, 3%IrO_x/NCNT, 4%IrO_x/NCNT, and 5%IrO_x/NCNT, respectively.

For comparison, 3%IrO_x/CNT was prepared by the similar method with that of IrO_x/NCNT except using CNT as the support.

3. Results and discussion

3.1. Characterization of catalysts

The existence form of the iridium species was analyzed by electron microscopy. From Fig. 1, the iridium-based nanoparticles (black dots) are highly dispersed on the NCNT and the average particle size is ca. 1.2 nm (Fig. 1b). The dispersion of iridium species on NCNT was further confirmed by HRSTEM. As displayed in Fig. 1c, the iridium-based nanoparticles (white dots) are well distributed onto the NCNT and no obvious aggregation of iridium oxide can be observed. The species of iridium was identified by HAADF-STEM. As demonstrated in Fig. 1d, the space between lattice fringes is 0.222 nm and 0.201 nm, indicating (111) lattice plane of metal Ir (PDF#06-0598) and (210) lattice plane of IrO_2 (PDF#15-0870), respectively. Therefore, the species of iridium was denoted as IrO_x.

The coordination environment and chemical valence of Ir species in 3%IrO_x/NCNT was studied by X-ray absorption fine structure (XAFS) (Fig. 2). The Ir L_{III}-edge XANES spectrum of 3%IrO_x/NCNT falls in between that of Ir foil and IrO_2, suggesting that the chemical valence of Ir species is between 0 and +4 (Fig. 2a). The most possible existential state of iridium species should be metal iridium coated by an iridium oxide shell. The FT-EXAFS spectrum in R space of Ir shows three peaks at ca. 2.01 Å, 2.3 Å, and 2.69 Å, which can be related to Ir-O/N, Ir-Cl, and Ir-Ir path, respectively (Fig. 2b). It can be noted that the peak position of Ir-O/N bond in the 3%IrO_x/NCNT shifts slightly negatively compared with that of Ir-O bond in the IrO_2, indicating coordination effect between N and Ir atoms. Based on the fitting curve in Fig. 2c, the coordination numbers of Ir-O/N, Ir-Cl, and Ir-Ir are 4.2, 2.8, and 5.5, respectively. The chemical valence of iridium species was further detected by XPS. As exhibited in Fig. 2d, the Ir 4f XPS in 3%IrO_x/CNT shows two Ir4f peaks at ca. 61.4 and 64.4 eV [19,20], which can be fitted into Ir^0 $4f_{7/2}$ (60.9 eV), Ir^{4+} $4f_{7/2}$ (61.5 eV), Ir^0 $4f_{5/2}$ (63.9 eV), and Ir^{4+} $4f_{5/2}$ (64.5 eV) [21–23]. The N 1s spectrum in 3%IrO_x/NCNT can be fitted into pyridinic-N (56.2%), pyrrolic-N (31.5%), and quaternary nitrogen (12.3%) (Fig. S1) [24].

3.2. HER performance

The electrocatalytic HER performance of IrO_x/NCNT was first studied in 0.5 M H_2SO_4 with Ohmic drop correction. As depicted in Fig. 3a, 3%IrO_x/CNT needs an overpotential (η_{10}) of 29 mV at 10 mA cm^{-2}, lower than that of 20% Pt/C (35 mV). The HER performance can be prominently improved by supporting iridium oxide onto the N-doped CNT. The overpotential at 10 mA cm^{-2} for 1%IrO_x/NCNT, 2%IrO_x/NCNT, 3%IrO_x/NCNT, 4%IrO_x/NCNT, and 5%IrO_x/NCNT is 17, 12, 8, 8, and 8 mV, respectively. The 3%IrO_x/NCNT shows higher HER activity than most catalysts reported previously in acidic media (Table S1). For convenience, the Tafel slope is described as positive values. The Tafel slope for 20% Pt/C, 3%IrO_x/CNT, 1%IrO_x/NCNT, 2%IrO_x/NCNT, 3%IrO_x/NCNT, 4%IrO_x/NCNT, and 5%IrO_x/NCNT is 30, 27, 15, 11, 10, 10, and 10 mV/decade, respectively (Fig. S2). The lower Tafel slope of 10 mV dec^{-1} for 3%IrO_x/NCNT indicates the HER superiority as compared with 20% Pt/C and 3%IrO_x/CNT. This Tafel slope implies a Tafel-step determined pathway that most probably works in the 3%IrO_x/NCNT catalyst.

The electrocatalytic HER performance of IrO_x/NCNT was further studied in 1 M KOH. As exhibited in Fig. 3b, unlike in the acidic condition, 3%IrO_x/CNT shows lower HER activity than 20% Pt/C in alkaline media. The introduction of nitrogen onto CNT can notably improve the HER activity of iridium oxide. The overpotential at 10 mA cm^{-2} for 20% Pt/C, 3%IrO_x/CNT, 1%IrO_x/NCNT, 2%IrO_x/NCNT, 3%IrO_x/NCNT, 4%IrO_x/NCNT, and 5%IrO_x/NCNT is 51, 98, 62, 45, 35, 32, and 28 mV, respectively, demonstrating that the 3%IrO_x/NCNT exhibits more superior HER activity than most catalysts reported previously (Table S2). The Tafel slopes are then plotted in Fig. S3, which demonstrates that 3%IrO_x/NCNT has a smaller Tafel slope (40 mV dec^{-1}) than 20% Pt/C (60 mV dec^{-1}), 3%IrO_x/CNT (145 mV dec^{-1}), 1%IrO_x/NCNT (68 mV dec^{-1}), and 2%IrO_x/NCNT (58 mV dec^{-1}). The Tafel slope of 40 mV dec^{-1} suggests that the HER process on 3%IrO_x/NCNT might likely follow the Heyrovsky rate-determining-step mechanism. In addition, a series of control experiments with high Ir content on NCNT indicate that the HER electrocatalysis processes a similar route with that on 3%IrO_x/NCNT [25].

The electrocatalytic HER performance of IrO_x/NCNT was further investigated in 0.1 M KOH. The LSV curves of the 20% Pt/C, 3%IrO_x/CNT, 1%IrO_x/NCNT, 2%IrO_x/NCNT, 3%IrO_x/NCNT, 4%IrO_x/NCNT, and 5%IrO_x/NCNT electrodes are exhibited in Fig. 3c. 3%IrO_x/NCNT, 4%IrO_x/NCNT and 5%IrO_x/NCNT show very positive overpotentials of ca. 44 mV to deliver 10 mA cm^{-2}, which is lower than that of 20% Pt/C (154 mV), 3%IrO_x/CNT (108 mV), 1%IrO_x/NCNT (102 mV), and 2%IrO_x/NCNT (67 mV). The Tafel plots are depicted in Fig. S4, indicating that the 3%IrO_x/NCNT (96 mV dec^{-1}) shows lower Tafel slope than 20% Pt/C (201 mV dec^{-1}), 3%IrO_x/CNT (222 mV dec^{-1}), 1%IrO_x/NCNT (148 mV dec^{-1}), and 2%IrO_x/NCNT (141 mV dec^{-1}). In addition, the 3%IrO_x/NCNT shows a comparable Tafel slope to 4%IrO_x/NCNT (92 mV dec^{-1}), and 5%IrO_x/NCNT (89 mV dec^{-1}), implying favorable HER kinetics via a Volmer–Heyrovsky pathway or a different reaction mechanism [26].

The HER activities were further evaluated in 1.0 M phosphate buffer solution (PBS) with pH of 7.0 (Fig. 3d). Comparatively, the catalytic performance of 3%IrO_x/CNT and commercial Pt/C was also studied. The Pt/C exhibits a large η_{10} of 258 mV and a Tafel slope of 333 mV dec^{-1} (Fig. S5). The 3%IrO_x/CNT shows higher electro-

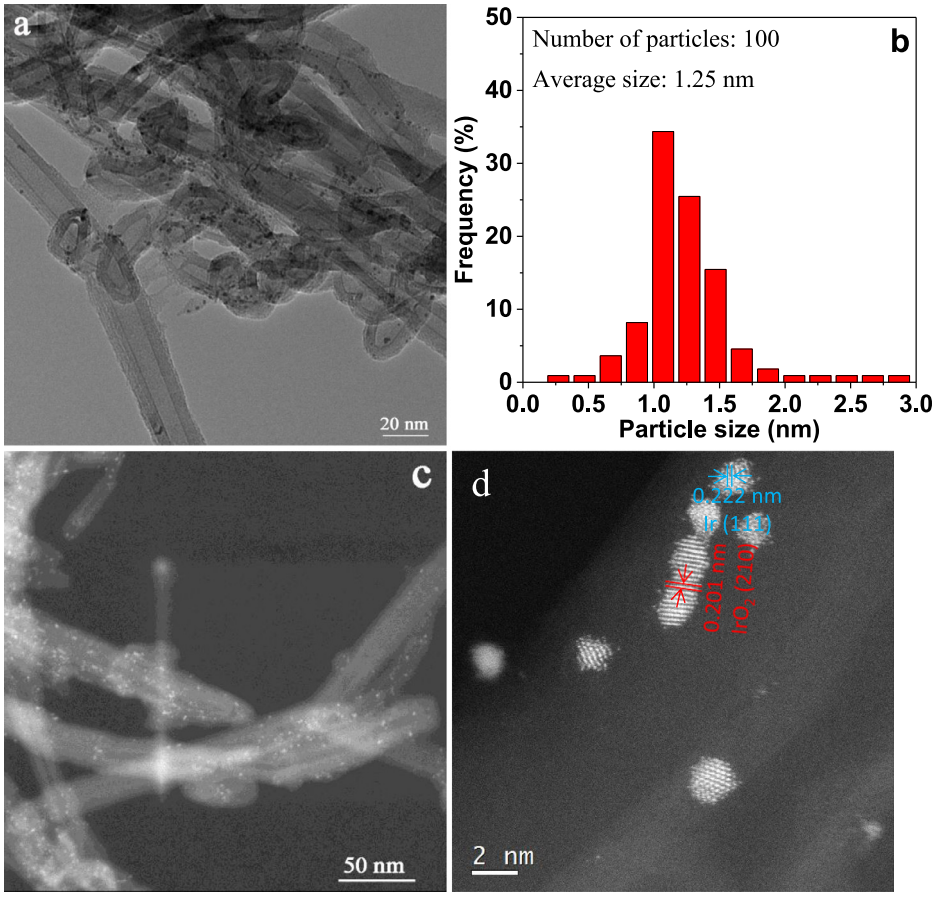

Fig. 1. (a) TEM image, (b) the histogram of size distribution, (c) HRSTEM image, and (d) HAADF-STEM image of 3%IrO_x/NCNT.

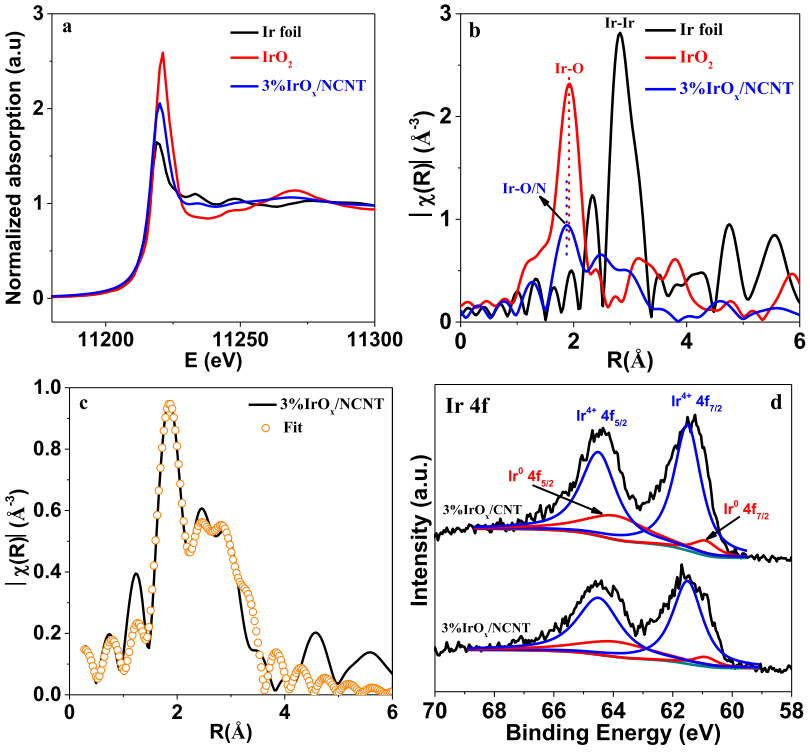

Fig. 2. (a) Ir XANES spectra and (b) Ir EXAFS spectra of 3%IrO_x/NCNT, Ir foil, and IrO_2. (c) Corresponding Ir L-edge EXAFS fitting. (d) Ir 4f XPS spectra of 3%IrO_x/CNT and 3%IrO_x/NCNT.

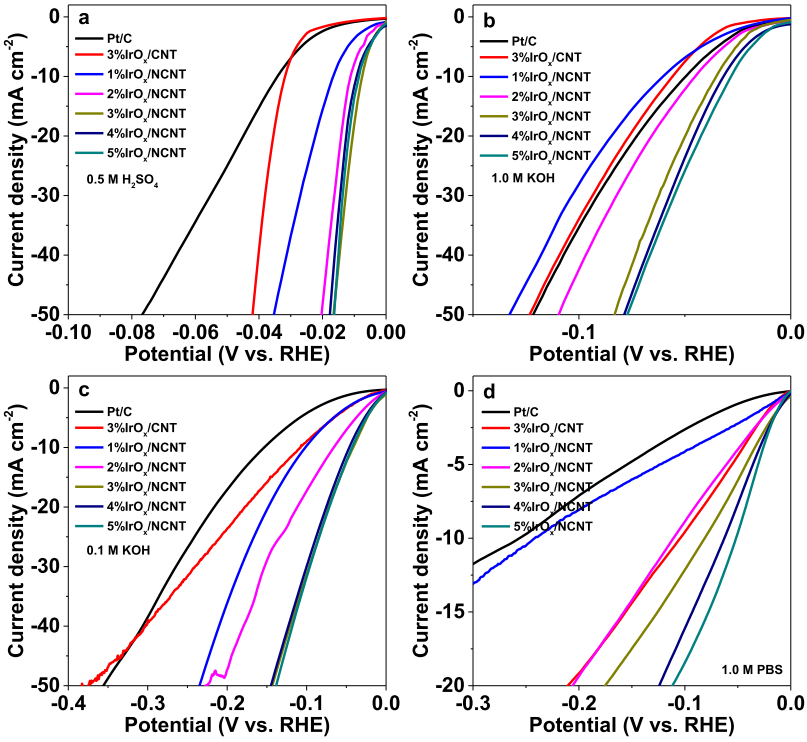

Fig. 3. (a) LSV curves in 0.5 M H_2SO_4. (b) LSV curves in 1 M KOH. (c) LSV curves in 0.1 M KOH. (d) LSV curves in 1 M PBS.

chemical HER activity than Pt/C, over which the η_{10} is 104 mV and the Tafel slope is 192 mV dec^{-1}. N-doping onto the CNT can significantly increase HER activity. In addition, higher Ir loadings can achieve higher HER activity. The 3%IrO$_x$/NCNT delivers a very low η_{10} of 82 mV, far surpassing that of the Pt/C. The Tafel slope is gradually decreased with increasing Ir loadings, implying the improved HER kinetics with the increase of Ir loadings (Fig. S5). The Tafel slope of 151 mV dec^{-1} suggests that the hydrogen evolution process on 3%IrO$_x$/NCNT might follow the Volmer mechanism [27].

The HER stability of 3%IrO$_x$/NCNT is evaluated by prolonged electrolysis at constant potentials in various electrolytes. As illustrated in Fig. S6, the 3%IrO$_x$/NCNT can maintain 80.8%, 62.8%, 76.6%, and 91.7% of the original current after reaction for 15 h in 0.5 M H_2SO_4, 1 M KOH, 0.1 M KOH, and 1 M PBS, respectively, demonstrating good HER stability in these media.

3.3. OER performance

The electrochemical activities of the samples towards OER were first assessed in 1.0 M KOH. As revealed in Fig. 4a, 3%IrO$_x$/CNT shows the lowest OER activity among the measured samples, even lower than commercial IrO_2 nanoparticles. The OER activity can be remarkably improved by supporting iridium oxide onto N-doped CNT, suggesting positive effect of N-doping towards OER. To reach 10 mA cm^{-2} current density, the as-prepared 3%IrO$_x$/NCNT requires an overpotential of only 241 mV, which is 29, 58, 7, and 7 mV less than those of IrO_2 nanoparticles, 3%IrO$_x$/CNT, 1%IrO$_x$/NCNT, and 2%IrO$_x$/NCNT, respectively. It can be observed that the 3%IrO$_x$/NCNT exhibits higher OER activity than most catalysts reported previously in alkaline media (Table S3). In addition, the 3%IrO$_x$/NCNT shows a turnover frequency (TOF) of 4.56 s^{-1} at an overpotential of 300 mV, which is 57 and 6 times higher than that of commercial IrO_2 and 3%IrO$_x$/CNT. Moreover, the Tafel plots indicate that 3%IrO$_x$/NCNT shows a lower Tafel slope of 40 mV/decade than IrO_2 (46 mV/decade) and 3%IrO$_x$/CNT (49 mV/decade), implying efficient electron and mass transfer. Tafel slope of 40 mV dec^{-1} for 3%IrO$_x$/NCNT suggests that the second electron transfer is the rate-determining step [28].

The electrochemical OER activities of the samples were further studied in 0.5 M H_2SO_4. The representative polarization curves are plotted in Fig. 4c. As expected, the IrO_2 catalyst exhibits a low overpotential of 313 mV at 10 mA cm^{-2} in acidic electrolyte. Meanwhile, the as-prepared 3%IrO$_x$/CNT electrocatalyst shows a relatively large overpotential of 369 mV. Similar to the case of alkaline OER, the electrocatalytic activity can be prominently enhanced by supporting IrO$_x$ onto NCNT. The OER overpotential for 1%IrO$_x$/NCNT, 2%IrO$_x$/NCNT, 3%IrO$_x$/NCNT, 4%IrO$_x$/NCNT, and 5%IrO$_x$/NCNT at 10 mA cm^{-2} is 310, 295, 285, 279, and 279 mV, respectively. Tafel plots depicted in Fig. 4d shows a small Tafel slope of 52 mV/decade for 3%IrO$_x$/NCNT, smaller than that for commercial IrO_2 (56 mV/decade), 3%IrO$_x$/CNT (96 mV/decade), 1%IrO$_x$/NCNT (65 mV/decade), and 2%IrO$_x$/NCNT (62 mV/decade). The Tafel slope of 52 mV/decade for 3%IrO$_x$/NCNT implies that the second electron transfer might be the rate-determining step in acidic OER process [28,29].

The electrocatalytic OER performance of IrO$_x$/NCNT was further studied in 1 M PBS electrolyte with pH of 7.0. As shown in Fig. 4e, 3%IrO$_x$/NCNT exhibits better OER performance than 3%IrO$_x$/CNT. To reach 10 mA cm^{-2}, 3%IrO$_x$/NCNT needs an overpotential of 376 mV, while 3%IrO$_x$/CNT needs 391 mV. 3%IrO$_x$/NCNT shows higher OER performance than commercial IrO_2 (η_{10} of 422 mV). The Tafel slope of 3%IrO$_x$/NCNT is 200 mV/decade, lower than those of commercial IrO_2 (254 mV/decade), 3%IrO$_x$/CNT (223 mV/decade), 1%IrO$_x$/NCNT (373 mV/decade), and 2%IrO$_x$/NCNT (230 mV/decade). The lower Tafel slope can offer a more prominently enhanced OER rate with increased overpotentials.

The OER stability of 3%IrO$_x$/NCNT was assessed in various electrolytes (Fig. S7). The current density shows a slight degradation during a long period of 25 h and it can maintain 79.7% of initial value in 1 M KOH, while it can maintain 83.7% of initial value in 0.5 M H_2SO_4 after 25 h, implying good OER stability in both acidic and alkaline conditions. In addition, 3%IrO$_x$/NCNT also shows stable OER in neutral PBS (Fig. S7).

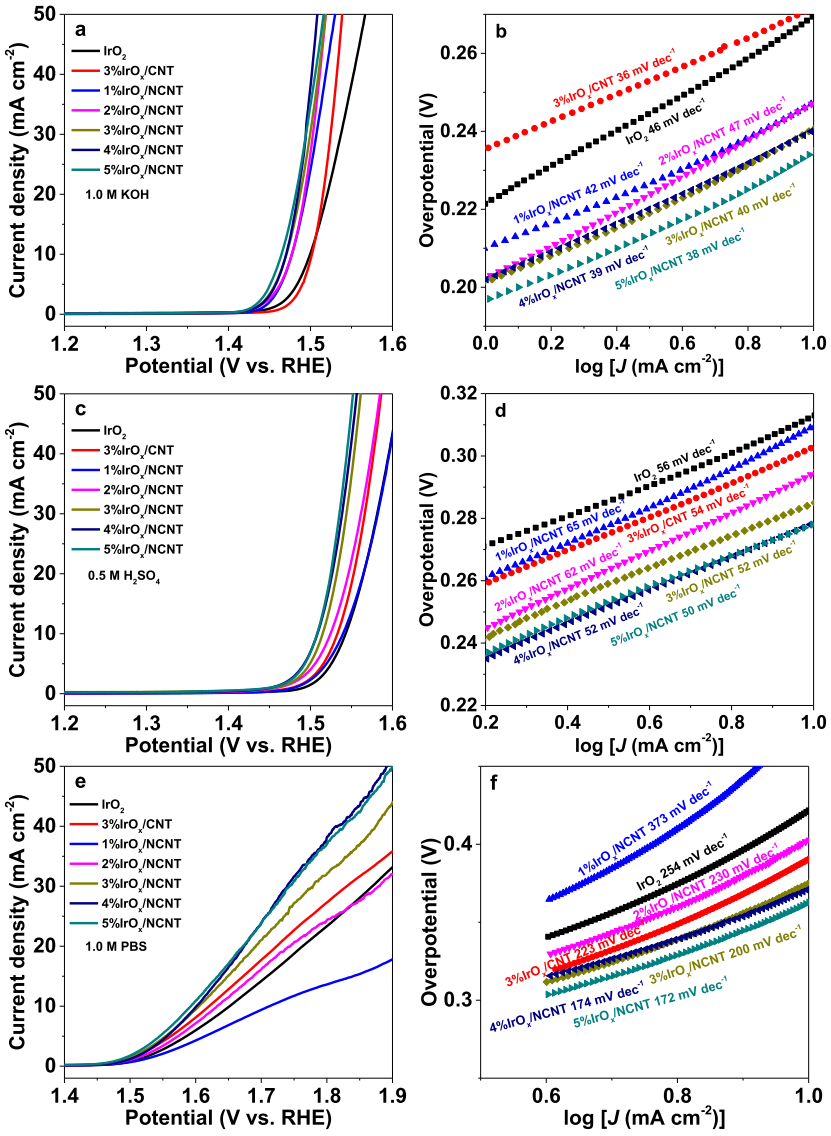

Fig. 4. (a) LSV curves in 1.0 M KOH. (b) Tafel plots. (c) LSV curves in 0.5 M H_2SO_4. (d) Tafel plots. (e) LSV curves of in 1 M PBS. (f) Tafel plots.

3.4. Overall water splitting performance

Due to high bifunctional HER/OER activities and stability of 3%IrO_x/NCNT, it was used as the cathode and anode to assemble an electrolyzer with two-electrode configuration for overall water splitting in 0.5 M H_2SO_4, 1.0 M KOH, and 1 M PBS. As exhibited in Fig. 5, the combination electrolyzer needs a potential of 1.487 V, 1.523 V, and 1.854 V to reach 10 mA cm^{-2} in 0.5 M H_2SO_4, 1.0 M KOH, and 1 M PBS, respectively, which surpass most bifunctional electrocatalysts in alkaline electrolytes (Table S4). Furthermore, the activity can be well maintained for 12 h in acidic and neutral media, indicating the promising application prospect in electrocatalytic water splitting systems. After stability tests, no detectable Ir is found in 0.5 M H_2SO_4 and 1 M PBS, while less than 0.1% of initial Ir is dissolved into 1.0 M KOH.

3.5. ORR performance

The electrochemical ORR performance was assessed in 0.1 M KOH. As displayed in Fig. 6a, prominent cathodic peaks for ORR can be observed for 3%IrO_x/CNT and 3%IrO_x/NCNT in O_2-saturated 0.1 M KOH, which are absent in N_2-saturated one. In addition, the peak position for 3%IrO_x/NCNT is more positive than 3%IrO_x/CNT, implying higher ORR activity of the former. RDE measurements are further employed to assess the ORR performance of these as-prepared samples. Compared with 3%IrO_x/CNT, the IrO_x/NCNT samples show higher ORR activity (Fig. 6b), indicating favorable role of N-doping onto CNT. The ORR half-wave potential of 3%IrO_x/NCNT is 0.757 V, lower than the Pt/C electrocatalyst (0.842 V). The 3%IrO_x/NCNT shows a smaller Tafel slope (65 mV/decade) at low overpotential than 3%IrO_x/CNT (84 mV/decade), demonstrating that the rate-determining step should be protonation of O^{2-} (Fig. S8) [30]. The number of electrons involved per O_2 (n) in the ORR over the 3%IrO_x/NCNT is measured. As shown in Fig. S9, the n-value is around 3.7 at the potentials ranging from 0.2 to 0.6 V, indicating that the four-electron ORR process is dominated. The ORR stability of 3%IrO_x/NCNT was evaluated (Fig. 6c). After continuous operation for 21 h, 90.8% of the original current density is remained for the 3%IrO_x/NCNT, far better than commercial Pt/C (only 62.3% of original current density reservation after 14 h) (Fig. S10). In addition, compared with Pt/C, the 3%IrO_x/NCNT exhibits better tolerance to carbon monoxide poisoning in alkaline solutions (Fig. S11).

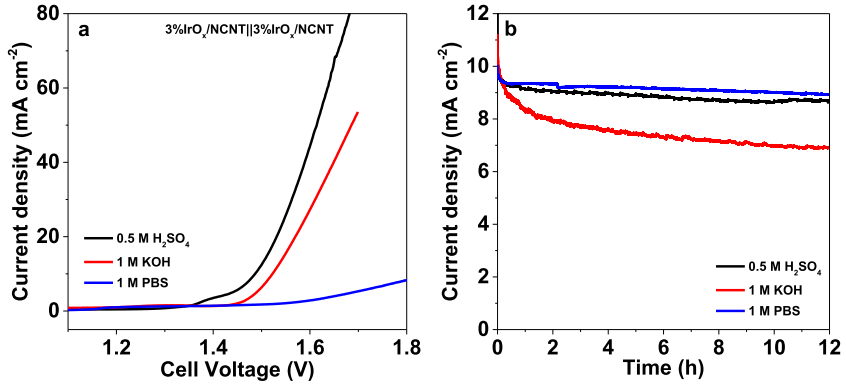

Fig. 5. (a) LSV curves of 3%IrO$_x$/NCNT||3%IrO$_x$/NCNT water splitting systems. (b) Chronoamperometry tests of the overall water splitting device consisting of 3%IrO$_x$/NCNT||3%IrO$_x$/NCNT.

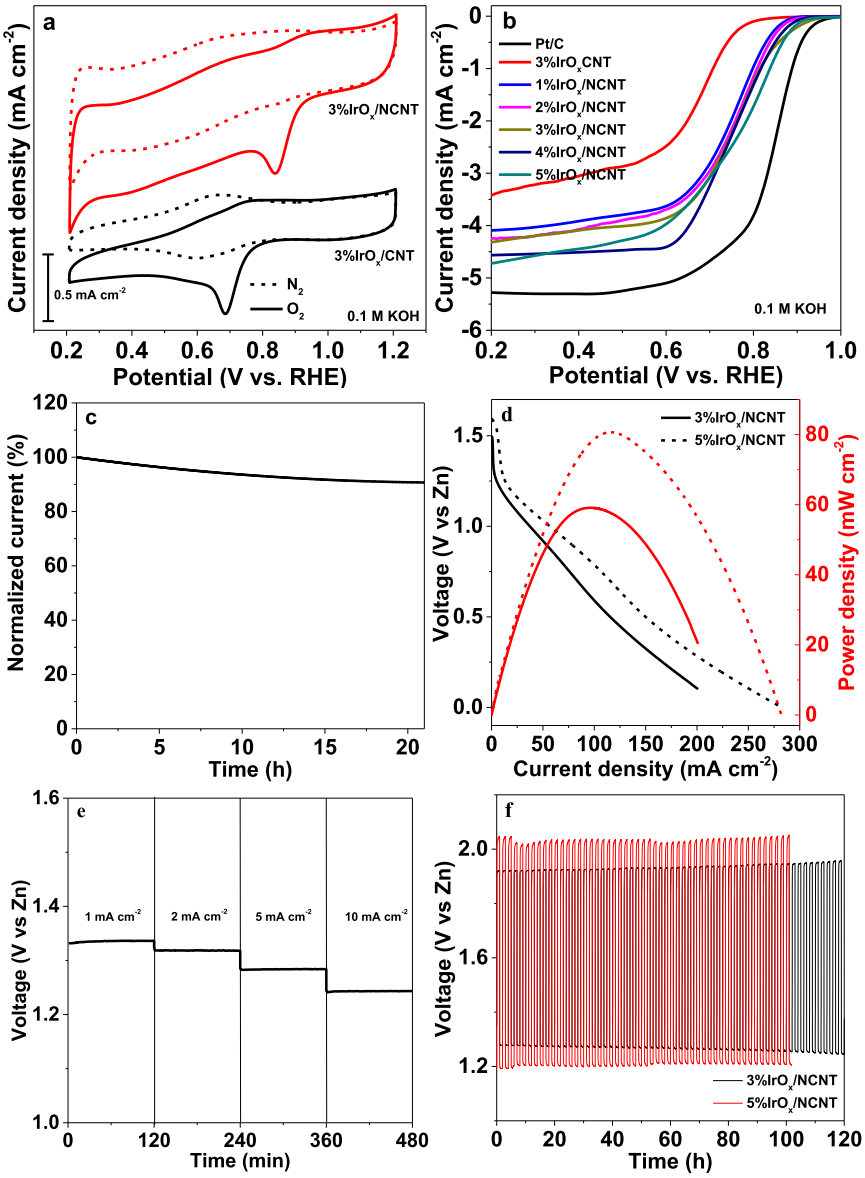

Fig. 6. (a) CV curves of 3%IrO$_x$/CNT and 3%IrO$_x$/NCNT. (b) ORR polarization curves of 20% Pt/C, 3%IrO$_x$/CNT, 1%IrO$_x$/NCNT, 2%IrO$_x$/NCNT, 3%IrO$_x$/NCNT, 4%IrO$_x$/NCNT, and 5%IrO$_x$/NCNT. (c) Chronoamperometric response of 3%IrO$_x$/NCNT. (d) Discharge curves of Zn–air batteries. (e) Discharge tests at different current densities on 3%IrO$_x$/NCNT-based Zn–air battery. (f) Galvanostatic discharge-charge cycling profiles at 5 mA cm^{-2}.

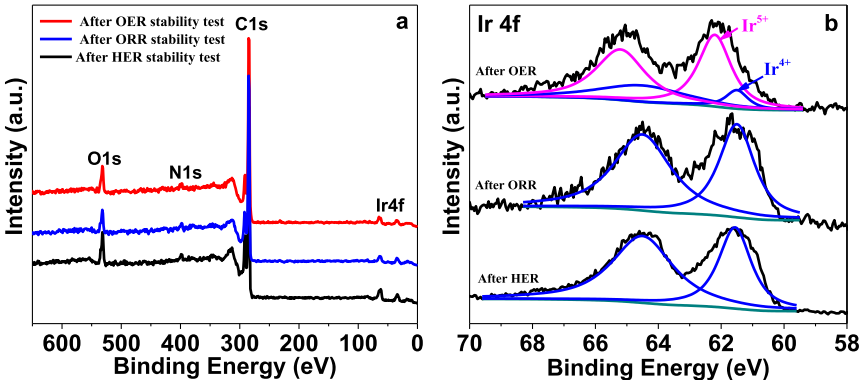

Fig. 7. (a) XPS survey spectra, and (b) high-resolution Ir4f XPS spectra of the used 3%IrO_x/NCNT catalyst after HER, ORR and OER stability test in 0.5 M H_2SO_4, 0.1 M KOH, and 0.5 M H_2SO_4, respectively.

3.6. Zn–air battery performance

Since the IrO_x/NCNT can effectually catalyze oxygen electrode reactions, a Zn–air battery was assembled using 3%IrO_x/NCNT or 5%IrO_x/NCNT as the oxygen electrode catalyst. The 3%IrO_x/NCNT-based battery and 5%IrO_x/NCNT-based battery show an open circuit voltage of 1.5 and 1.6 V, and a maximum power density of 59.3 and 80.7 mW cm^{-2}, respectively (Fig. 6d). Galvanostatic discharge test exhibits that the voltage is 1.34 V at 1 mA cm^{-2}, 1.32 V at 2 mA cm^{-2}, 1.28 V at 5 mA cm^{-2}, and 1.24 V at 10 mA cm^{-2} with excellent stability on 3%IrO_x/NCNT-based battery (Fig. 6e). The charge–discharge cycling stability tests were studied at 5 mA cm^{-2}. The batteries with 3%IrO_x/NCNT and 5%IrO_x/NCNT air-cathodes show superior stability with a small voltage gap of ca. 0.65 and 0.80 V, respectively. After cycling for more than 100 h (Fig. 6f), the 3%IrO_x/NCNT and 5%IrO_x/NCNT air-cathodes demonstrate excellent stability, indicating that the IrO_x/NCNT catalyst is an outstanding bifunctional catalyst for rechargeable Zn–air batteries.

3.7. Active sites for HER, OER, and ORR

To investigate the active sites for HER, OER, and ORR on 3%IrO_x/NCNT, we characterize the catalyst after electrochemical stability tests. After tests, the samples were collected, washed, and then dried under vacuum at 40°C for 12 h. As displayed in Fig. 7, C, O, N and Ir are the main elements. The surface valence state of Ir in the 3%IrO_x/NCNT after HER stability test is mainly presented as +4, suggesting that the ultra-small Ir atoms are very active, which can be oxidized by the electrochemically generated oxygen. This finding indicates that the active sites for HER might be IrO_2 or partially reduced IrO_x [31]. However, for commercial IrO_2, the HER activity is very poor no matter in acidic, alkaline and neutral media (Fig. S12). Therefore, the cooperation between IrO_2 and NCNT should be responsible for the high-efficiency HER. Similarly, the surface valence state of Ir in the 3%IrO_x/NCNT after ORR stability test is mainly presented as +4, implying that IrO_2 is the main active site for ORR. However, pure IrO_2 shows poor ORR activity (Fig. S13).[32] The enhanced ORR activity should be due to the synergistic effect between IrO_2 and NCNT. The synergistic effect should be twofold: one is that the charge transfer resistance (R_{ct}) and diffusion resistance of IrO_2 are decreased by supporting it onto NCNT as shown in the EIS plots (Fig. S14); the other is that the electronic structure of IrO_2 might be affected by the coordination with N elements in NCNT as revealed by XAFS results. After OER test, a great deal of Ir^{5+} is detected, indicating that Ir^{5+} is a key intermediate during oxygen evolution process.

4. Conclusions

In summary, we have reported a simple, fast, and general synthetic approach to fabricate ultrafine iridium oxide onto N-doped CNT for boosting hydrogen/oxygen evolution catalysis. The as-prepared 3%IrO_x/NCNT catalyst exhibits trifunctional HER, OER and ORR performance due to the synergistic effect between IrO_2 and NCNT. For HER, it shows ultra-low overpotentials of 8 mV, 35 mV, 44 mV, and 82 mV at 10 mA•cm^{-2} in 0.5 M H_2SO_4, 1 M KOH, 0.1 M KOH, and 1 M PBS, respectively. For OER, it exhibits low overpotentials of 241 mV, 285 mV, and 376 mV at 10 mA•cm^{-2} in 1.0 M KOH, 0.5 M H_2SO_4, and 1 M PBS, respectively. The excellent hydrogen/oxygen evolution ability of 3%IrO_x/NCNT enables it as a bifunctional electrocatalyst for electrochemical overall water splitting, while the oxygen evolution/reduction ability makes it as a bifunctional electrocatalyst for zinc–air battery devices. The as-assembled water splitting device using 3%IrO_x/NCNT as anode and cathode and as-assembled zinc–air battery using 3%IrO_x/NCNT as cathode demonstrates high efficiency and durability, suggesting the feasibility of 3%IrO_x/NCNT in electrochemical energy conversion and storage.

CRediT author statement

Jingqi Guan: Supervision, Conceptualization, Methodology, Data curation, Writing- Original draft preparation.
Ning Liu: Investigation and Characterization.
Yin Wang: Investigation.
Qiaoqiao Zhang: Investigation

Declaration of Competing Interest

☒ The authors declare that they have no known competing financial interests or personal relationships that could have appeared to influence the work reported in this paper.

Acknowledgments

This work was supported by the National Natural Science Foundation of China (22075099), Natural Science Foundation of Jilin Province (20180101291JC).

Supplementary materials

Supplementary material associated with this article can be found, in the online version, at doi:10.1016/j.electacta.2021.138215.

References

[1] Y. Liu, C. Xiao, P. Huang, M. Cheng, Y. Xie, Regulating the charge and spin ordering of two-dimensional ultrathin solids for electrocatalytic water splitting, Chem 4 (2018) 1263–1283.

[2] J. Liu, Q. Ma, Z. Huang, G. Liu, H. Zhang, Recent progress in graphene-based noble-metal nanocomposites for electrocatalytic applications, Adv. Mater. 31 (2019) 1800696.

[3] H. Sun, Z. Yan, F. Liu, W. Xu, F. Cheng, J. Chen, Self-supported transition-metal-based electrocatalysts for hydrogen and oxygen evolution, Adv. Mater. 32 (2020) 1806326.

[4] L. Jiao, H.-L. Jiang, Metal-organic-framework-based single-atom catalysts for energy applications, Chem 5 (2019) 786–804.

[5] R. Matheu, P. Garrido-Barros, M. Gil-Sepulcre, M.Z. Ertem, X. Sala, C. Gimbert–Surinach, A. Llobet, The development of molecular water oxidation catalysts, Nat. Rev. Chem. 3 (2019) 331–341.

[6] Y. Li, Y. Sun, Y. Qin, W. Zhang, L. Wang, M. Luo, H. Yang, S. Guo, Recent advances on water-splitting electrocatalysis mediated by noble-metal-based nanostructured materials, Adv. Energy Mater. 10 (2020) 1903120.

[7] B. Zhang, T. Fan, N. Xie, G. Nie, H. Zhang, Versatile applications of metal single-atom @ 2D material nanoplatforms, Adv. Sci. 6 (2019) 1901787.

[8] Y. Li, Z. Dong, L. Jiao, Multifunctional transition metal-based phosphides in energy-related electrocatalysis, Adv. Energy Mater. 10 (2020) 1902104.

[9] J. Kim, H.-E. Kim, H. Lee, Single-atom catalysts of precious metals for electrochemical reactions, ChemSusChem 11 (2018) 104–113.

[10] W.-H. Lai, L.-F. Zhang, W.-B. Hua, S. Indris, Z.-C. Yan, Z. Hu, B. Zhang, Y. Liu, L. Wang, M. Liu, R. Liu, Y.-X. Wang, J.-Z. Wang, Z. Hu, H.-K. Liu, S.-L. Chou, S.-X. Dou, General pi-electron-assisted strategy for Ir, Pt, Ru, Pd, Fe, Ni single-atom electrocatalysts with bifunctional active sites for highly efficient water splitting, Angew. Chem., Int. Ed. 58 (2019) 11868–11873.

[11] Y. Ping, R.J. Nielsen, W.A. Goddard III, The reaction mechanism with free energy barriers at constant potentials for the oxygen evolution reaction at the IrO_2 (110) surface, J. Am. Chem. Soc. 139 (2017) 149–155.

[12] L.C. Seitz, C.F. Dickens, K. Nishio, Y. Hikita, J. Montoya, A. Doyle, C. Kirk, A. Vojvodic, H.Y. Hwang, J.K. Norskov, T.F. Jaramillo, A highly active and stable IrOx/$SrIrO_3$ catalyst for the oxygen evolution reaction, Science 353 (2016) 1011–1014.

[13] H. Jang, J. Lee, Iridium oxide fabrication and application: a review, J. Energy Chem. 46 (2020) 152–172.

[14] L. Yang, X. Zeng, W. Wang, D. Cao, Recent progress in MOF-derived, heteroatom-doped porous carbons as highly efficient electrocatalysts for oxygen reduction reaction in fuel cells, Adv. Funct. Mater. 28 (2018) 1704537.

[15] Z. Lei, T. Wang, B. Zhao, W. Cai, Y. Liu, S. Jiao, Q. Li, R. Cao, M. Liu, Recent progress in electrocatalysts for acidic water oxidation, Adv. Energy Mater. 10 (2020) 2000478.

[16] H. Xu, D. Cheng, D. Cao, X.C. Zeng, A universal principle for a rational design of single-atom electrocatalysts, Nat. Catal. 1 (2018) 339–348.

[17] Y. Shao, Z. Jiang, Q. Zhang, J. Guan, Progress in nonmetal-doped graphene electrocatalysts for the oxygen reduction reaction, ChemSusChem 12 (2019) 2133–2146.

[18] X. Wu, B. Feng, W. Li, Y. Niu, Y. Yu, S. Lu, C. Zhong, P. Liu, Z. Tian, L. Chen, W. Hu, C.M. Li, Metal-support interaction boosted electrocatalysis of ultrasmall iridium nanoparticles supported on nitrogen doped graphene for highly efficient water electrolysis in acidic and alkaline media, Nano Energy 62 (2019) 117–126.

[19] X. Wen, L. Bai, M. Li, J. Guan, Ultrafine iridium oxide supported on carbon nanotubes for efficient catalysis of oxygen evolution and oxygen reduction reactions, Mater. Today Energy 10 (2018) 153–160.

[20] J. Guan, D. Li, R. Si, S. Miao, F. Zhang, C. Li, Synthesis and demonstration of subnanometric iridium oxide as highly efficient and robust water oxidation catalyst, ACS Catal. 7 (2017) 5983–5986.

[21] H.G.S. Casalongue, M.L. Ng, S. Kaya, D. Friebel, H. Ogasawara, A. Nilsson, In situ observation of surface species on iridium oxide nanoparticles during the oxygen evolution reaction, Angew. Chem. Int. Ed. 53 (2014) 7169–7172.

[22] W. Sun, X. Tian, J. Liao, H. Deng, C. Ma, C. Ge, J. Yang, W. Huang, Assembly of a highly active iridium-based oxide oxygen evolution reaction catalyst by using metal-organic framework self-dissolution, ACS Appl. Mater. Interfaces 12 (2020) 29414–29423.

[23] A. Lim, J. Kim, H.J. Lee, H.-J. Kim, S.J. Yoo, J.H. Jang, H.Y. Park, Y.-E. Sung, H.S. Park, Low-loading IrO_2 supported on Pt for catalysis of PEM water electrolysis and regenerative fuel cells, Appl. Catal. B 272 (2020) 118955.

[24] J. Guan, Z. Duan, F. Zhang, S.D. Kelly, R. Si, M. Dupuis, Q. Huang, J.Q. Chen, C. Tang, C. Li, Water oxidation on a mononuclear manganese heterogeneous catalyst, Nat. Catal. 1 (2018) 870–877.

[25] Y. Cheng, S. Lu, F. Liao, L. Liu, Y. Li, M. Shao, Rh-MoS_2 nanocomposite catalysts with Pt-like activity for hydrogen evolution reaction, Adv. Funct. Mater. 27 (2017) 1700359.

[26] M.D. Hossain, Z. Liu, M. Zhuang, X. Yan, G.-L. Xu, C.A. Gadre, A. Tyagi, I.H. Abidi, C.-J. Sun, H. Wong, A. Guda, Y. Hao, X. Pan, K. Amine, Z. Luo, Rational design of graphene-supported single atom catalysts for hydrogen evolution reaction, Adv. Energy Mater. 9 (2019) 1803689.

[27] J. Guan, X. Wen, Q. Zhang, Z. Duan, Atomic rhodium catalysts for hydrogen evolution and oxygen reduction reactions, Carbon 164 (2020) 121–128.

[28] M.S. Burke, M.G. Kast, L. Trotochaud, A.M. Smith, S.W. Boettcher, Cobalt-iron (Oxy)hydroxide oxygen evolution electrocatalysts: the role of structure and composition on activity, stability, and mechanism, J. Am. Chem. Soc. 137 (2015) 3638–3648.

[29] D.K. Bediako, C. Costentin, E.C. Jones, D.G. Nocera, J.-M. Saveant, Proton–electron transport and transfer in electrocatalytic films. Application to a cobalt-based O_2-evolution catalyst, J. Am. Chem. Soc. 135 (2013) 10492–10502.

[30] L. Bai, Z. Duan, X. Wen, J. Guan, Bifunctional atomic iron-based catalyst for oxygen electrode reactions, J. Catal. 378 (2019) 353–362.

[31] L. Li, B. Wang, G. Zhang, G. Yang, T. Yang, S. Yang, S. Yang, Electrochemically modifying the electronic structure of $IrO_{(2)}$nanoparticles for overall electrochemical water splitting with extensive adaptability, Adv. Energy Mater. 10 (2020) 2001600.

[32] P.P. Patel, O.I. Velikokhatnyi, S.D. Ghadge, P.H. Jampani, M.K. Datta, D. Hong, J.A. Poston, A. Manivannan, P.N. Kumta, Highly active robust oxide solid solution electro-catalysts for oxygen reduction reaction for proton exchange membrane fuel cell and direct methanol fuel cell cathodes, Int. J. Hydrog. Energy 42 (2017) 24079–24089.